DESIGN CONTROL SUMMARY

CLIENT:	Progress Energy	UNIT NO.:	1 & 2
PROJECT NAME:	LNP COL Application		
PROJECT NO.:	07-3935	[X]	NUCLEAR SAFETY-RELATED
CALC NO.:	LNG-0000-XDC-001, Rev. 2	[ ]	NOT NUCLEAR SAFETY RELATED
TITLE:	Effect of Grouting on Groundwater Flow Regime		
EQUIPMENT NO.:			

IDENTIFICATION OF PAGES ADDED/REVISED/SUPERSEDED/VOIDED AND REVIEW METHOD

INPUTS/ASSUMPTIONS	
X	VERIFIED
	UNVERIFIED

REVIEW METHOD:	Detailed	REV:	2
STATUS:		DATE FOR REV:	
PREPARER:	Melih Demirkan	DATE:	11/19/2008
REVIEWER:	Xiaosong Xia	DATE:	11/19/2008
APPROVER:	Mike Edwards	DATE:	11/19/2008

IDENTIFICATION OF PAGES ADDED/REVISED/SUPERSEDED/VOIDED AND REVIEW METHOD

INPUTS/ASSUMPTIONS	
	VERIFIED
	UNVERIFIED

REVIEW METHOD:		REV:	
STATUS:		DATE FOR REV:	
PREPARER:		DATE:	
REVIEWER:		DATE:	
APPROVER:		DATE:	

IDENTIFICATION OF PAGES ADDED/REVISED/SUPERSEDED/VOIDED AND REVIEW METHOD

INPUTS/ASSUMPTIONS	
	VERIFIED
	UNVERIFIED

REVIEW METHOD:		REV:	
STATUS:		DATE FOR REV:	
PREPARER:		DATE:	
REVIEWER:		DATE:	
APPROVER:		DATE:	

NOTE: PRINT AND SIGN IN THE SIGNATURE AREAS

TABLE OF CONTENTS

Effect of Grouting on Groundwater Flow Regime (Revision 2)

Objective:

The objective of this calculation is to determine how altering the Levy Nuclear Plant (LNP) groundwater flow regime by flow barriers (i.e., grouting) could affect groundwater velocity below and around the periphery of the grouted zone. This evaluation will be performed by comparing the groundwater flow regime before and after the construction of the grouted zone and during the construction dewatering.

Background:

As a part of the dewatering program, 75 feet of the Avon Park Formation will be grouted and a diaphragm wall will be installed to provide flow barrier (i.e., bathtub) during NI construction. The dewatering system will lower the potentiometric surface below the depth of excavation. The grouted zone will also have supplemental advantages such as inhibiting the karst development by means of reducing the dissolution activity within the grouted zone. The increase in the density of a 75-feet thick grouted zone underneath the NI may alter the groundwater flow characteristics namely, groundwater velocity around the periphery of this zone.

In a three-dimensional groundwater model, the pre-grouting site conditions were simulated in steady state flow regime. Subsequently, in order to evaluate how grouting will impact the groundwater velocity, a three-dimensional model was also created to determine the influence of grouted zone on the local groundwater regime. Based on the results of the two models, groundwater heads, velocities, and directions were compared prior to and after the grouting.

Finally, a three dimensional model of the excavation dewatering of LNP construction was also evaluated in order to predict the influence of excavation dewatering on the local groundwater regime.

References:

1. CH2M Hill, 2008, "Properties of Subsurface Layers for Engineering Analysis," Calculation No. LNG-0000-X7C-025, Rev. 0, May, 2008.
2. Paul C. Rizzo Associates, 2008a. "Design of Excavation Dewatering System" Calculation No: LNG-0000-XEC-001, Rev.1, May 2008.
3. Paul C. Rizzo Associates, 2008b. "Computer Program Verification and Validation Information, Visual MODFLOW 4.2, MODFLOW, MODPATH, ZONEBUDGET," January 6, 2008.
4. Young D.,F., Munson B.,R., and Okiishi T. H., 2001, "A Brief introduction to Fluid Mechanics" 2nd Ed., Wiley & Sons, NY.
5. Santamarina C. J. (2001) "Soil Behavior at the Micro-scale: Particle Forces", *Proceeding Symposium Soil Behavior and Soft Ground Construction in honor of Charles C. Ladd*, MIT, Cambridge MA.

Design Inputs:

The groundwater levels in the surficial aquifer have been measured between El. 41.3 and 42.54 feet above mean sea level (ft amsl) in March 2007. These levels are near the ground surface (approx. El. 43 ft amsl). Groundwater elevations in the Upper Floridan aquifer (UFA) (monitored via deep wells) were slightly lower but were also very close to the ground surface in March 2007 (El. 40.73 to 42.21 ft amsl) (Rizzo 2008a). Potentiometric heads measured in the Upper Floridan aquifer and used in 3D modeling are shown in ***Figure 1***.

As regards the subsurface stratification, the silty sand overburden deposit varies in thickness, but is approximately 67 feet thick in the vicinity of LNP (CH2M Hill 2008). The overburden deposits underlain by Avon Park limestone formation are moderately to highly permeable. The permeability and thickness of the subsurface layers used in the 3D models are given in Table 1 (Rizzo 2008a).

The permeability values included in this model represents the karst features. The effect of karst infillings is reflected through site specific permeability

Consistent with field observations and the previously reported values, the Avon Park Formation extends to El. -450 ft. The base of the model was conservatively defined to be El. -450 ft amsl (493 ft bgs), which represents the base of the UFA and the top of the Middle Confining Unit (MCU). The base of the model is defined as a no-flow boundary.

Table 1. Layer Properties employed in the modeling

Layer Description	Elevation (ft NAVD 88)		Thickness (ft)	Hydraulic Conductivity (ft/day)
	Top	Bottom		
Silty Sand Deposits	+43	-24	67	9.2
Avon Park Limestone	-24	-54	30	13.9
Avon Park Limestone – higher permeability	-54	-99	45	27.8
Avon Park Limestone – higher permeability	-99	-150	51	27.8
Avon Park Limestone – higher permeability	-150	-250	100	27.8
Avon Park Limestone	-250	-450	200	13.9
Grouted zone*	-24	-99	75	0.027
Diaphragm Wall	43	-54	-	0.003

* Target permeability of grouted zone is 1 Lugeon (0.027 ft/d).

Methodology:

A numerical simulation was performed to model the pre-construction (unaltered) groundwater conditions. In this 3D finite difference groundwater flow model, spatially-variable boundary conditions and hydraulic conductivities, and multiple geologic layers are used under existing potentiometric conditions. The modeling was performed using the U.S. Geological Survey's MODFLOW 2000 software, which is contained in a graphical user interface (GUI) software package called Visual MODFLOW Premium Version 4.2. This software has been verified and validated (Rizzo 2008b).

The finite-difference grid is square in shape and represents an area 3,850 feet on a side. The total model area has been discretized (i.e., divided) into 400 rows, 400 columns, and 6 layers which creates 960,000 cells in the model domain. The model area is discretized finer in the center of the model where NI is located. The inner portion of the model area (400 ft x 400 ft) is divided into 3.5 ft x 3.5 ft grid cells. The model domain extends vertically from El. +43 ft amsl down to El. -450 ft; the total thickness of the model domain is 493 feet. The domain is divided into six horizontal layers including the surficial aquifer and the upper permeable portion of the Avon Park Formation (***Table 1***).

Constant-head boundaries were assigned to the outer edges of the model, based on the interpolated hydraulic heads. Details of the head interpolation are given by Rizzo 2008a. The potentiometric surfaces for March 2007 are slightly above average, so the estimated boundary conditions are conservative for calculating groundwater flow into the excavation.

In addition to the model with natural potentiometric heads (pre-grouting), a 3D model simulating the subsurface conditions after the construction has been completed. The second model uses the same input parameters for aquifer materials outside the construction zone. The primary differences between two models are the presence of the high density – low permeability grouted zone, diaphragm wall, and the low-permeability foundation of the NI.

In a third model, a 3D simulation of the excavation dewatering was also created using same input parameters as the model created for the dewatering system design with an exception of grouted zone permeability which is conservatively taken as 0.28 ft/d. This permeability represents a grout condition with less than one year of production. The grouted zone is expected to reach its target properties (i.e., permeability) one year after production. This period required for final permeability is typical for grouting application. The design of excavation dewatering system has been reported in detail by Rizzo 2008a.

During dewatering process, the maximum drawdown will occur when the excavation is deepest (-24 ft amsl) and the RCC has not been emplaced. Maximum seepage rates, maximum pumping rates, and maximum hydraulic gradients will also occur when the excavation has reached its deepest point and placement of the RCC has not occurred. In the transient flow model for

dewatering modeling, the -24 ft amsl elevation has been reached in the 6th and the last stress period. Therefore, the hydraulic heads and groundwater velocities used for comparison purposes are taken from the last stress period. See the details of the dewatering modeling in Rizzo 2008a.

All three models (i.e., pre-grouting, dewatering and post-grouting) contain 9 observation wells, located around the NI, which are shown in ***Figure 2***. One of these wells is located at the center of the NI area (observation well C in Figure 2). Two wells are placed at each side of the NI area (e.g., E1 and E2 at the east side as observation wells East1 and East2), placed 12.5 ft and 62.5 ft respectively from the proposed diaphragm wall location. With two observation points at each side of the NI, the differences in the groundwater flow pattern can be assessed in terms of hydraulic heads and gradients around NI at these observation wells.

Hydraulic heads and groundwater velocities are determined at the same location in both models in two different subsurface zones. Zone A is designated as the zone between elevations -24 and -99 ft msl. Zone B is designated as the zone between elevations -99 ft and -250 ft msl. The model can predict three components of the groundwater velocity, namely x-, y-, and z- direction, therefore these three components are reported. In addition, the resultant velocity, which is designated as total velocity ($V_{t\,max}$) is also reported.

In karst terrains, the erosion and movement of the soil particles contained in the rock cavities and fissures may cause subsidence of the overlaying rock and soil layers. Therefore, as final stage in this calculation, minimum velocity that can remove the clay particle (lower range of clay particle as 1 micron) in the infill zones of Avon Park was determined using the approach explained in Attachment A. This velocity is compared with the velocities observed from the post-grouting model.

Results:

The comparative results of the three dimensional finite difference analyses are given in ***Table 2***. These results indicate the maximum observed hydraulic heads and the maximum groundwater velocity in x, y and z directions at pre-construction and post-construction conditions at Zone A and Zone B. Typical schematics of simulation outputs for pre-construction and post-construction conditions are shown in ***Figures 3 and 4***, respectively.

Both models resulted in same hydraulic heads in Zone A and Zone B. More importantly, relative low groundwater velocities observed throughout the model indicate that the change in the hydraulic gradient due to grouting is not sufficient to impact the groundwater regime.

Maximum groundwater velocity ($V_{t\,max}$) is observed in Zone B at observation well W1 as 0.162 ft/d (5.7E-7 m/sec) in post-construction model (***Table 2***). The maximum increase (40 percent) in the total groundwater velocity is obtained in Zone B of observation well W1 between pre- and post- construction conditions.

The maximum hydraulic head difference between pre-construction and dewatering is determined as 0.7 ft located 12.5 ft from the NI footprint at Zone A. The hydraulic head changes due to dewatering vary between 0.5 ft. and 0.7 ft. around NI (Table 3).

Maximum groundwater velocity increase due to dewatering was observed at observation well C in Zone B. This maximum dewatering velocity observed around the NI footprint was 1.14 ft/day (4E-6 cm/sec) (Table 3).

Santamarina (2001) indicated that a minimum groundwater velocity of 1E-3 m/sec (283 ft/d) is needed to cause detachment of any particle. This velocity requirement is significantly higher than observed velocity of 0.162 ft/d (5.7E-7 m/sec).

Additionally, based on *Equation 9* of Attachment A, the threshold groundwater velocity in the vertical direction (z- direction) that can remove a clay particle in 1 micron is calculated as 0.26 ft/d (See Attachment A for sample calculation). As mentioned above, the total maximum groundwater velocity is calculated 0.162 ft/d (***Table 2***). This grain size (1 micron) falls into lower range clay size materials which typically have grain size between 0.001 mm to 0.005 mm. The parameters required to calculate the particle diameter given by Equation (9) are as follows: G_s of the soil particle is taken as 2.65, μ_w is 1.003 E-3 N sec/m^2 at 20 °C and γ_w is 10 kN/m^3.

Conclusions:

The change in the groundwater flow regime at the Avon Park Formation due to grouting is judged to be insignificant with regards to having any impact on the LNP foundation. An analysis considering the normal forces on a soil particle (i.e., drag force and self weight of the particle) has been performed. The results indicate that a groundwater velocity of 0.26 ft/day is necessary to transport the smallest (1 micron) clay particle. In a more advanced evaluation of the normal and tangential forces on a soil particle, including electrical attraction forces, it was shown (Santamarina, 2001) that a minimum of 283 ft/day groundwater velocity may be necessary to cause a detachment of any particle.

In the post-construction model, a maximum groundwater velocity of 0.162 ft/day was determined. The increase in groundwater velocity due to LNP construction is not large enough to move the particles of any infilled zones, and therefore additional erosion activity is negligible.

Table 2 Hydraulic heads, groundwater velocity from pre-grouting and post-grouting analyses

Observation Well		C			E1			E2			W1			W2		
		Pre	Post	Δ	Pre	Post	Δ	Pre	Post	Δ	Pre	Post	Δ	Pre	Post	Δ
Zone A	Max. Head (ft)	41.9	41.9	**0**	41.8	41.8	**0**	41.8	41.8	**0**	42	42	**0**	42	42	**0**
	$V_{x\,max}$ (ft/d)	-0.111	-1.00E-04	**0.111**	-0.1	-0.005	**0.095**	-0.112	-0.082	**0.030**	-0.109	0.004	**0.105**	-0.106	-0.074	**0.032**
	$V_{y\,max}$ (ft/d)	0.042	6.00E-04	**0.041**	0.04	0.03	**0.010**	0.039	0.038	**0.001**	0.042	-0.061	**0.019**	0.042	0.053	**0.011**
	$V_{z\,max}$ *(ft/d)	-0.038	-0.0002	**0.038**	-0.012	0.031	**0.019**	-0.014	-0.003	**0.011**	-0.012	-0.074	**0.062**	-0.014	-0.032	**0.018**
	$V_{t\,max}$ *(ft/d)	0.12	0.0002	**0.120**	0.117	0.042	**0.075**	0.12	0.091	**0.029**	0.118	0.097	**0.021**	0.116	0.097	**0.019**
Zone B	Max. Head (ft)	41.9	41.9	**0**	41.8	41.8	**0**	41.8	41.8	**0**	42	42	**0**	42	42	**0**
	$V_{x\,max}$ (ft/d)	-0.107	-0.117	**0.01**	-0.112	-0.12	**0.008**	-0.114	-0.102	**0.012**	-0.108	-0.139	**0.031**	-0.105	-0.101	**0.004**
	$V_{y\,max}$ (ft/d)	0.026	0.049	**0.023**	0.039	0.045	**0.006**	0.038	0.041	**0.003**	0.042	0.05	**0.008**	0.042	0.048	**0.006**
	$V_{z\,max}$ *(ft/d)	-0.03	0.002	**0.028**	-0.008	-0.036	**0.028**	-0.009	-0.001	**0.008**	-0.011	-0.068	**0.057**	-0.012	-0.031	**0.019**
	$V_{t\,max}$ *(ft/d)	0.119	0.13	**0.011**	0.119	0.133	**0.014**	0.121	0.11	**0.011**	***0.116***	***0.162***	**0.046**	0.114	0.117	**0.003**

Δ: Difference between Pre and Post conditions

*: The positive direction of V_z is upward, toward ground surface. Positive directions of V_x and V_y are shown in Figure 1.

Table 2 (cont.)

		N1			N2			S1			S2		
		Pre	Post	Δ	Pre	Post	Δ	Pre	Post	Δ	Pre	Post	Δ
Zone A	Max. Head (ft)	41.9	41.9	**0**	41.9	41.9	**0**	41.9	41.9	**0**	41.9	41.9	**0**
	$V_{x\,max}$ (ft/d)	-0.11	-0.142	**0.032**	-0.11	-0.12	**0.010**	-0.11	-0.12	**0.010**	-0.112	-0.119	**0.007**
	$V_{y\,max}$ (ft/d)	0.043	0.002	**0.041**	0.043	0.03	**0.013**	0.041	-0.001	**0.040**	0.039	0.022	**0.017**
	$V_{z\,max}$ (ft/d)	-0.04	-0.008	**0.032**	-0.04	-0.003	**0.037**	-0.012	-0.047	**0.035**	-0.014	-0.028	**0.014**
	$V_{t\,max}$ (ft/d)	0.119	0.143	**0.024**	0.119	0.13	**0.011**	0.12	0.12	**0.000**	0.119	0.125	**0.006**
Zone B	Max. Head (ft)	41.9	41.9	**0**	41.9	41.9	**0**	41.9	41.9	**0**	41.9	41.9	**0**
	$V_{x\,max}$ (ft/d)	-0.11	-0.126	**0.016**	-0.11	-0.12	**0.01**	-0.11	-0.119	**0.009**	-0.112	-0.118	**0.006**
	$V_{y\,max}$ (ft/d)	0.044	0.046	**0.002**	0.044	0.039	**0.005**	0.039	0.062	**0.023**	0.037	0.038	**0.001**
	$V_{z\,max}$ (ft/d)	-0.009	-0.012	**0.003**	-0.009	-0.001	**0.008**	-0.01	-0.041	**0.031**	-0.012	-0.026	**0.014**
	$V_{t\,max}$ (ft/d)	0.119	0.133	**0.014**	0.119	0.126	**0.007**	0.119	0.14	**0.021**	0.119	0.127	**0.008**

Table 3 Hydraulic heads, groundwater velocity from pre-grouting and dewatering analyses

Observation Well		C			E1			E2			W1			W2		
		Pre.	Dewat.	Δ	Pre.	Dewat.	Δ	Pre.	Dewat.	Δ	Pre.	Dewat.	Δ	Pre.	Dewat.	Δ
Zone A	Max. Head (ft)	41.9	N/A	**N/A**	41.8	41.2	**0.6**	41.8	41.3	**0.5**	42	41.4	**0.6**	42	41.5	**0.5**
	$V_{x\,max}$ (ft/d)	-0.111	N/A	**N/A**	-0.1	0.624	**0.524**	-0.112	0.269	**0.157**	-0.109	-0.82	**0.711**	-0.106	-0.47	**0.364**
	$V_{y\,max}$ (ft/d)	0.042	N/A	**N/A**	0.04	-0.231	**0.191**	0.039	-0.01	**0.029**	0.042	-0.072	**0.03**	0.042	0.012	**0.03**
	$V_{z\,max}$ (ft/d)	-0.038	N/A	**N/A**	-0.012	0.117	**0.105**	-0.014	0.05	**0.036**	-0.012	-0.04	**0.028**	-0.014	0.025	**0.011**
	$V_{t\,max}$ (ft/d)	0.119	N/A	**N/A**	0.117	0.68	**0.563**	0.12	0.27	**0.15**	0.118	0.82	**0.702**	0.116	0.47	**0.354**
Zone B	Max. Head (ft)	41.9	41.3	**0.7**	41.8	41.3	**0.5**	41.8	41.3	**0.5**	42	41.4	**0.6**	42	41.5	**0.5**
	$V_{x\,max}$ (ft/d)	-0.107	-0.108	**0.001**	-0.112	0.381	**0.269**	-0.114	0.203	**0.089**	-0.108	-0.675	**0.567**	-0.105	-0.449	**0.344**
	$V_{y\,max}$ (ft/d)	0.026	-0.06	**0.034**	0.039	-0.061	**0.022**	0.038	0.017	**0.021**	0.042	-0.021	**0.021**	0.042	0.025	**0.017**
	$V_{z\,max}$ (ft/d)	-0.03	1.14	**1.11**	-0.008	0.237	**0.229**	-0.009	0.093	**0.084**	-0.011	0.182	**0.171**	-0.012	0.087	**0.075**
	$V_{t\,max}$ (ft/d)	0.119	1.11	**0.991**	0.119	0.45	**0.331**	0.121	0.22	**0.099**	***0.116***	0.69	**0.574**	0.114	0.45	**0.336**

N/A: Not applicable because the section is grouted.

Δ: Difference between Pre-grouting (Pre.) and dewatering (Dewat.)

*: The positive direction of V_z is upward, toward ground surface. Positive directions of V_x and V_y are shown in Figure 1.

Table 3 (cont.)

		N1			N2			S1			S2		
		Pre.	Dewat.	Δ	Pre.	Dewat.	Δ	Pre.	Dewat.	Δ	Pre.	Dewat.	Δ
Zone A	Max. Head (ft)	41.9	41.2	**0.7**	41.9	41.3	**0.6**	41.9	41.2	**0.7**	41.9	41.3	**0.6**
	$V_{x\ max}$ (ft/d)	-0.11	-0.045	**0.065**	-0.11	-0.103	**0.007**	-0.11	-0.1	**0.01**	-0.112	-0.112	**0**
	$V_{y\ max}$ (ft/d)	0.043	-0.802	**0.759**	0.043	-0.433	**0.39**	0.041	0.937	**0.896**	0.039	0.546	**0.507**
	$V_{z\ max}$ (ft/d)	-0.04	0.097	**0.057**	-0.04	0.017	**0.023**	-0.012	0.101	**0.089**	-0.014	0.063	**0.049**
	$V_{t\ max}$ (ft/d)	0.119	0.81	**0.691**	0.119	0.45	**0.331**	0.12	0.95	**0.83**	0.119	0.56	**0.441**
Zone B	Max. Head (ft)	41.9	41.3	**0.6**	41.9	41.4	**0.5**	41.9	41.3	**0.6**	41.9	41.4	**0.5**
	$V_{x\ max}$ (ft/d)	-0.11	-0.1	**0.01**	-0.11	-0.103	**0.007**	-0.11	-0.104	**0.006**	-0.112	0.111	**0.001**
	$V_{y\ max}$ (ft/d)	0.044	-0.552	**0.508**	0.044	-0.352	**0.308**	0.039	0.65	**0.611**	0.037	0.453	**0.416**
	$V_{z\ max}$ (ft/d)	-0.009	0.261	**0.252**	-0.009	0.114	**0.105**	-0.01	0.328	**0.318**	-0.012	0.152	**0.14**
	$V_{t\ max}$ (ft/d)	0.119	0.62	**0.501**	0.119	0.38	**0.261**	0.119	0.74	**0.621**	0.119	0.49	**0.371**

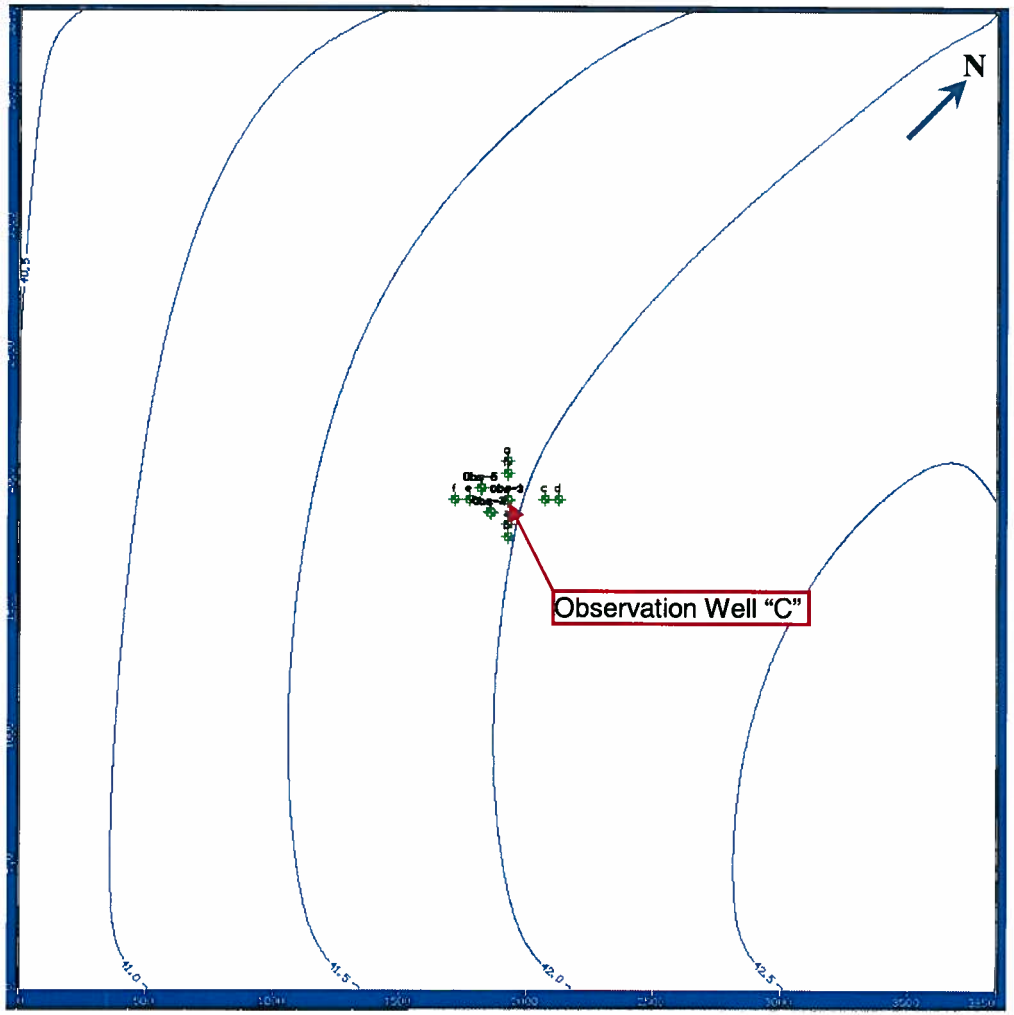

Figure 1 Pre-grouting model potentiometric heads at 193 ft. below ground surface (El. -150 ft.)

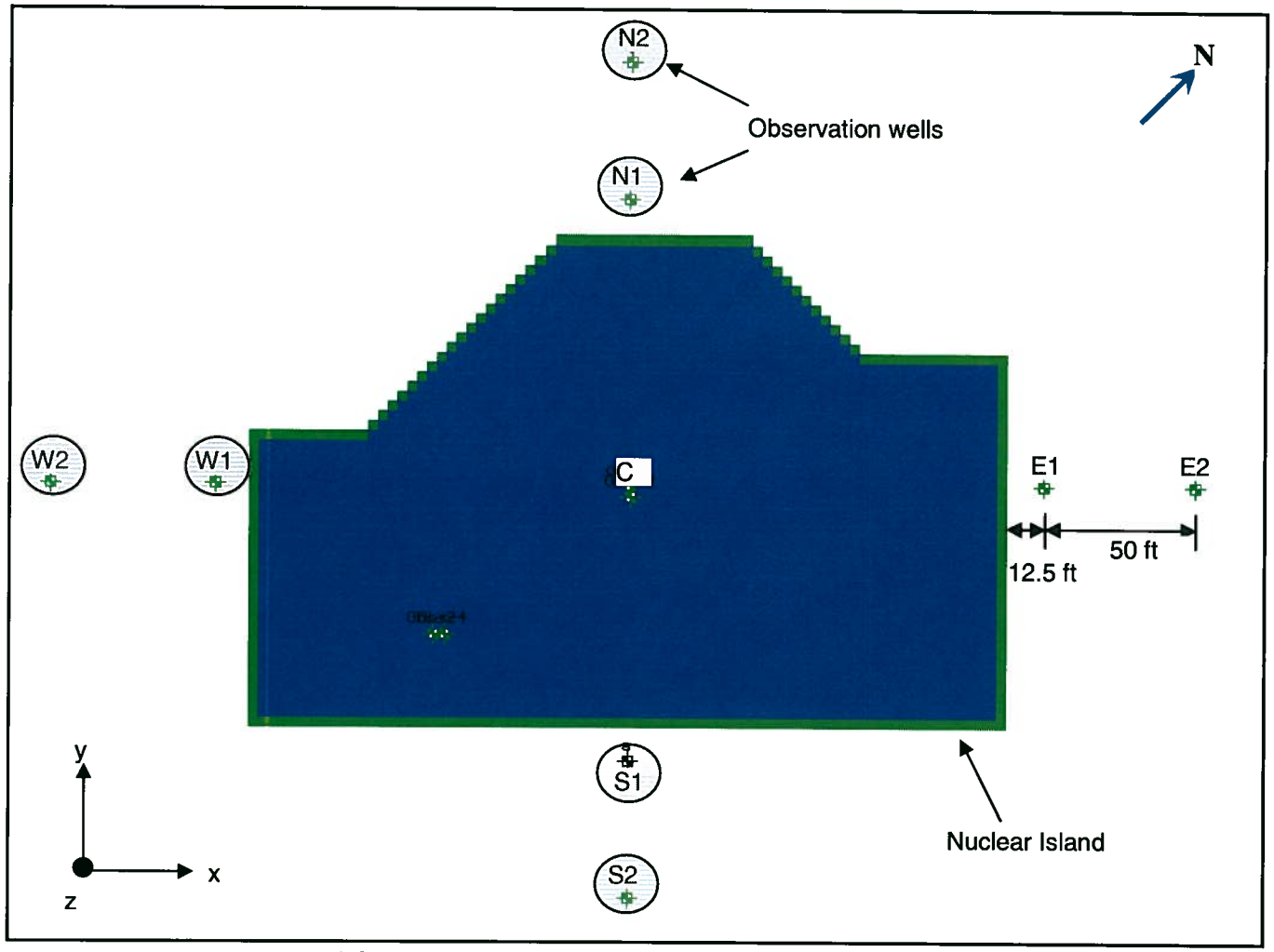

Figure 2 Observation well locations around NI

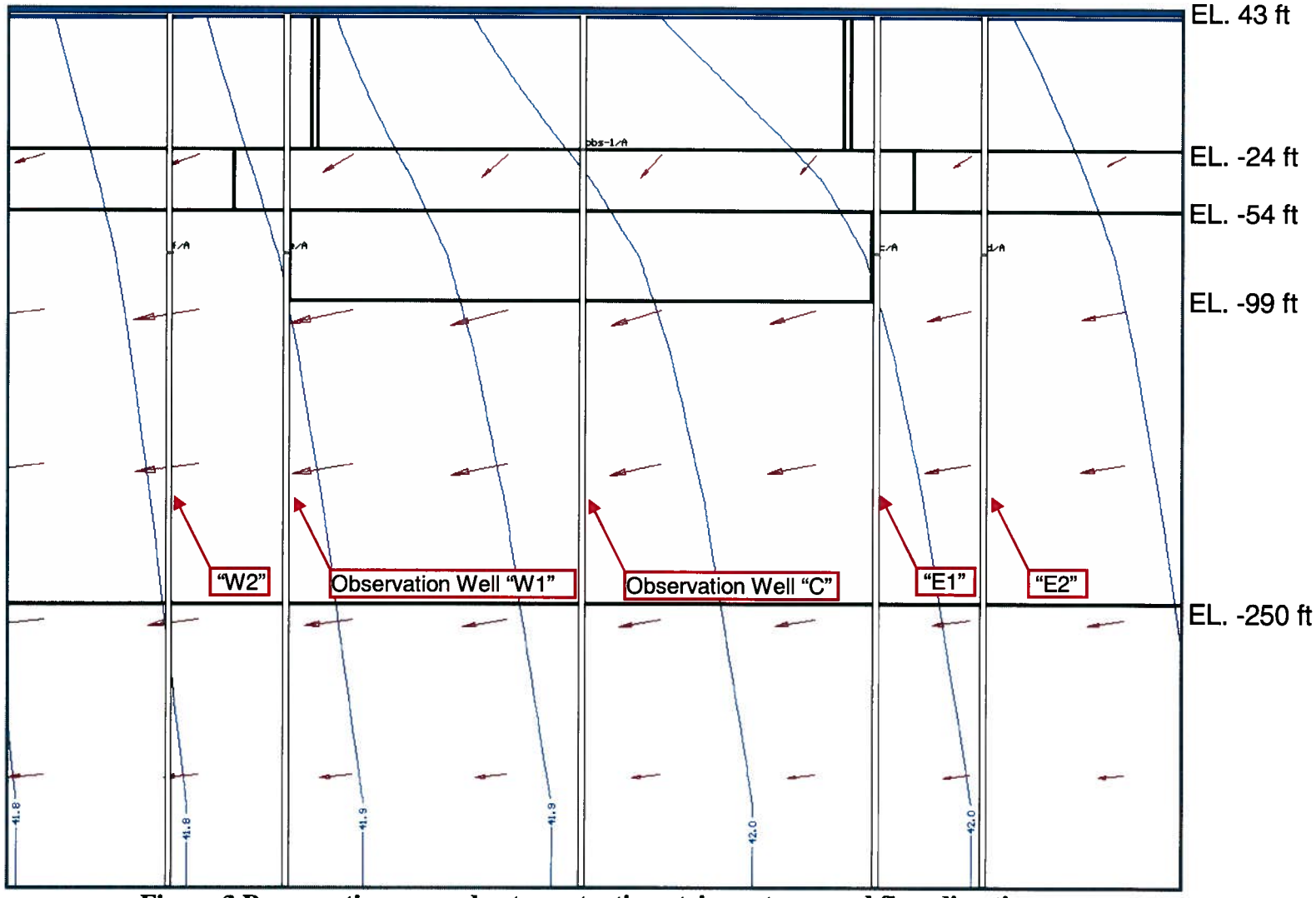

Figure 3 Pre-grouting groundwater potentiometric contours and flow directions

By:	MD	Date:	11/19/2008	Subject:	Effect of Grouting On	Sheet No.	15	of 27
By:	XS	Date:	11/19/08		Groundwater Flow Regime, Rev. 2	Project No.	07-3935	

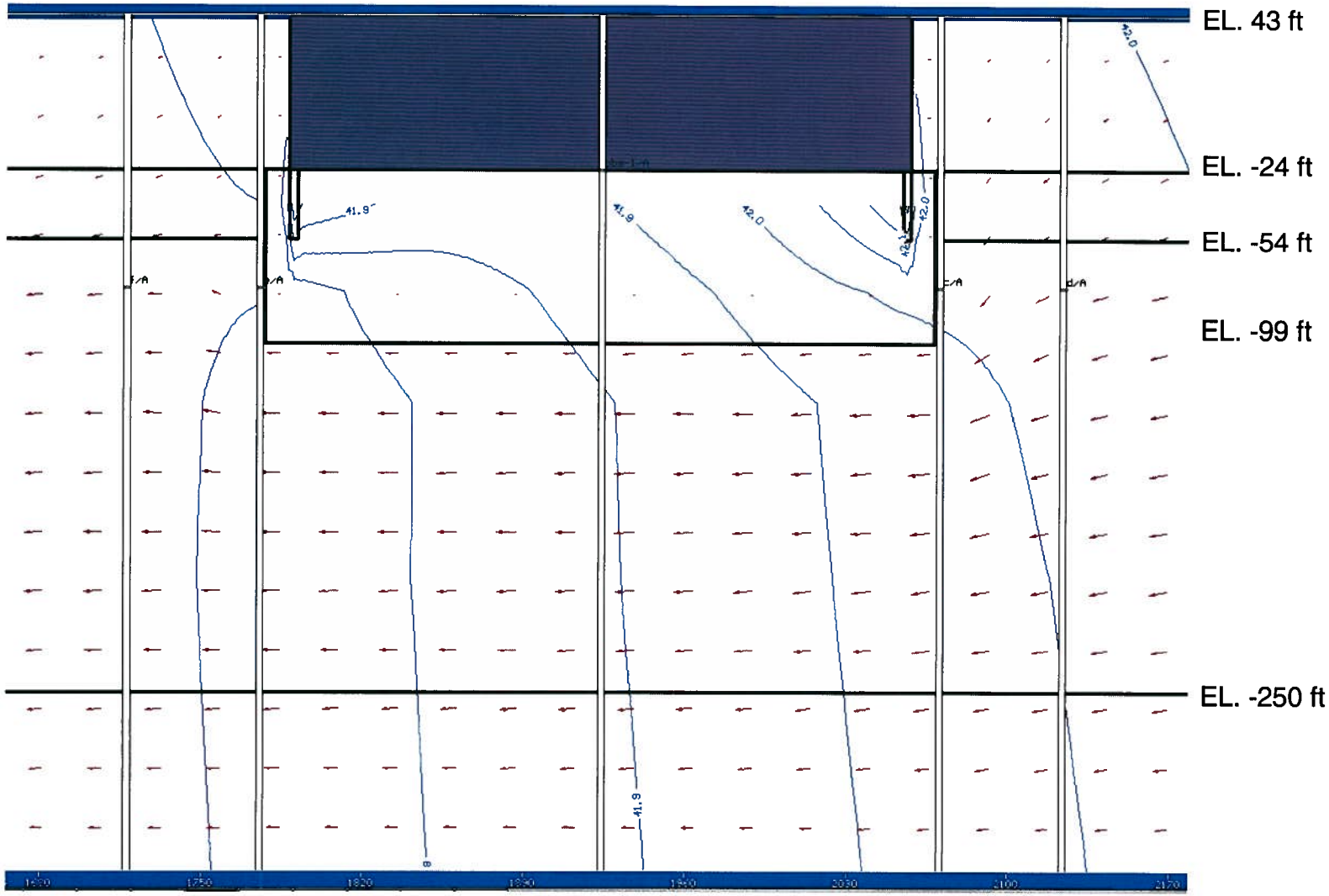

Figure 4 Post-grouting groundwater potentiometric contours and flow directions

ATTACHMENT A
Groundwater Velocity - Particle Size Evaluation

One of the major concerns associated with the change in the groundwater velocities within the Avon Park formation is the erosion and movement of the soil particles confined in the infilled zones. Soil particles move due to the drag forces induced by the flowing groundwater and this drag force can be determined by (Young et al. 2001):

$$D_f = \frac{1}{2}\,\rho_w V^2 \frac{\pi}{4} D^2 C_D \tag{1}$$

where D_f is the drag force (net force in the direction of flow due to pressure and shear forces) on the surface of the particle (kg m /sec^2), ρ_w is the density of the groundwater (kg/m^3), V is the groundwater velocity (m/sec), D is the particle diameter (m), C_D is the drag coefficient (dimensionless). In order to calculate the drag force, the following assumptions has been made:

- Soil particles have a spherical shape.
- The groundwater flow has a low Reynolds coefficient (Re<1) because of the smallness of the soil particles.

Based on the above assumptions, C_D is calculated as:

$$C_D = \frac{24}{Re} \tag{2}$$

where

$$Re = \frac{\rho_w V D}{\mu_w} \tag{3}$$

where μ_w is the viscosity of water (N/sec m). When *Equation (3)* is substantiated into *Equation (2)* and following the transfer of Equation (2) into *Equation (1)*, the drag force can be expressed as :

$$D_f = 3\,V\,\pi\,\mu_w\,D \tag{4}$$

In addition to drag force, the buoyancy force (F_b) of the surrounding water is acting against the weight of the soil particles (W). Based on the free body diagram of a soil particle following equilibrium is obtained:

$$D_f + F_b = W \tag{5}$$

where

$$F_b = \gamma_w \frac{\pi}{6} D^3 \tag{6}$$

where γ_w is the water unit weight (KN/m^3), and the weight of the particle can be obtained using:

$$W = G_s\,\gamma_w \frac{\pi}{6} D^3 \tag{7}$$

In *Equation (7)*, G_s is the specific gravity of the soil particle.

The arrangement of the *Equations (4)*, *(6)* and *(7)* using *Equation (5)* results in the particle diameter that will be removed due to the groundwater flow as:

$$D = \sqrt{\frac{18\,\mu_w\,V}{(G_s-1)\gamma_w}} \tag{8}$$

Equation (8) provides the maximum soil particle diameter that can be moved with certain groundwater velocity (*V*). *Equation (8)* can be re-written as to get the velocity that can remove particles in grain diameter "D":

$$V = \frac{D^2(G_s-1)\gamma_w}{18\,\mu_w} \tag{9}$$

Sample Calculations:

G_s =2.65,
μ_w = 1.003 E-3 N sec/m^2 at 20 °C,
γ_w = 10 kN/m^3 = 10,000 N/m^3
D = 0.001 mm

$$V = \frac{(1E-6)^2(2.65-1)\ x\ 10{,}000}{18\ x\ 1.003\ 10^{-3}}$$

V= 9.14 E-7 m/sec =0.26 ft/d

Particle size that can be removed by 1.14 ft/d = 4 E-6 m/sec

$$D = \sqrt{\frac{18\ x\ 1.003\ 10^{-3} x\ 4\ 10^{-6}}{(2.65-1)\ x\ 10{,}000}}$$

D= 0.000002 m= 2 micron

ATTACHMENT B
Selected References

A Brief Introduction to Fluid Mechanics

Second Edition

DONALD F. YOUNG
BRUCE R. MUNSON
Department of Aerospace Engineering
and Engineering Mechanics

THEODORE H. OKIISHI
Department of Mechanical Engineering
Iowa State University
Ames, Iowa, USA

JOHN WILEY & SONS, INC.

because of the viscous effects involved, the particle in the boundary layer experiences a loss of energy as it flows along. This loss means that the particle does not have enough energy to coast all of the way up the pressure hill (from C to F) and to reach point F at the rear of the cylinder. This kinetic energy deficit is seen in the velocity profile detail at point C, shown in Fig. 9.12*a*. Because of friction, the boundary layer fluid cannot travel from the front to the rear of the cylinder. (This conclusion can also be obtained from the concept that due to viscous effects the particle at C does not have enough momentum to allow it to coast up the pressure hill to F.)

V9.4 Snow drifts

Thus, the fluid flows against the increasing pressure as far as it can, at which point the boundary layer separates from (lifts off) the surface. This *boundary layer separation* is indicated in Fig. 9.12*a*. Typical velocity profiles at representative locations along the surface are shown in Fig. 9.12*b*. At the separation location (profile D), the velocity gradient at the wall and the wall shear stress are zero. Beyond that location (from D to E) there is reverse flow in the boundary layer.

As is indicated in Fig. 9.12*c*, because of the boundary layer separation, the average pressure on the rear half of the cylinder is considerably less than that on the front half. Thus, a large pressure drag is developed, even though (because of small viscosity) the viscous shear drag may be quite small.

The location of separation, the width of the wake region behind the object, and the pressure distribution on the surface depend on the nature of the boundary layer flow. Compared with a laminar boundary layer, a turbulent boundary layer flow has more kinetic energy and momentum associated with it because (1) the velocity profile is fuller, more nearly like the ideal uniform profile, and (2) there can be considerable energy associated with the swirling, random components of the velocity that do not appear in the time-averaged x component of velocity. Thus, as is indicated in Fig. 9.12*c*, the turbulent boundary layer can flow farther around the cylinder (farther up the pressure hill) before it separates than can the laminar boundary layer.

9.3 Drag

As was discussed in Section 9.1, any object moving through a fluid will experience a drag, $\mathcal{D}$—a net force in the direction of flow due to the pressure and shear forces on the surface of the object. This net force, a combination of flow direction components of the normal and tangential forces on the body, can be determined by use of Eqs. 9.1 and 9.2, provided the distributions of pressure, p, and wall shear stress, τ_w, are known. Only in very rare instances can these distributions be determined analytically.

Most of the information pertaining to drag on objects is a result of numerous experiments with wind tunnels, water tunnels, towing tanks, and other ingenious devices that are used to measure the drag on scale models. Typically, the result for a given shaped object is a drag coefficient, C_D, where

$$C_D = \frac{\mathcal{D}}{\frac{1}{2}\rho U^2 A} \tag{9.22}$$

and C_D is a function of other dimensionless parameters such as Reynolds number, Re, Mach number, Ma, Froude number, Fr, and relative roughness of the surface, ε/ℓ. That is,

$$C_D = \phi(\text{shape}, \text{Re}, \text{Ma}, \text{Fr}, \varepsilon/\ell)$$

9.3.1 Friction Drag

Friction drag, $\mathfrak{D}_f$, is that part of the drag that is due directly to the shear stress, τ_w, on the object. It is a function of not only the magnitude of the wall shear stress, but also of the orientation of the surface on which it acts. This is indicated by the factor $\tau_w \sin\theta$ in Eq. 9.1. For highly streamlined bodies or for low Reynolds number flow most of the drag may be due to friction.

The friction drag on a flat plate of width b and length ℓ oriented parallel to the upstream flow can be calculated from

$$\mathfrak{D}_f = \tfrac{1}{2}\rho U^2 b \ell C_{Df}$$

where C_{Df} is the friction drag coefficient. The value of C_{Df} is given as a function of Reynolds number, $\text{Re}_\ell = \rho U \ell/\mu$, and relative surface roughness, ε/ℓ, in Fig. 9.10 and Table 9.1.

Most objects are not flat plates parallel to the flow; instead, they are curved surfaces along which the pressure varies. The precise determination of the shear stress along the surface of a curved body is quite difficult to obtain. Although approximate results can be obtained by a variety of techniques (Refs. 1, 2), these are outside the scope of this text.

9.3.2 Pressure Drag

Pressure drag, $\mathfrak{D}_p$, is that part of the drag that is due directly to the pressure, p, on an object. It is often referred to as *form drag* because of its strong dependency on the shape or form of the object. Pressure drag is a function of the magnitude of the pressure and the orientation of the surface element on which the pressure force acts. For example, the pressure force on either side of a flat plate parallel to the flow may be very large, but it does not contribute to the drag because it acts in the direction normal to the upstream velocity. On the other hand, the pressure force on a flat plate normal to the flow provides the entire drag.

As previously noted, for most bodies, there are portions of the surface that are parallel to the upstream velocity, others normal to the upstream velocity, and the majority of which are at some angle in between. The pressure drag can be obtained from Eq. 9.1 provided a detailed description of the pressure distribution and the body shape is given. That is,

$$\mathfrak{D}_p = \int p \cos\theta \, dA$$

which can be rewritten in terms of the *pressure drag coefficient*, C_{Dp}, as

$$C_{Dp} = \frac{\mathfrak{D}_p}{\frac{1}{2}\rho U^2 A} = \frac{\int p \cos\theta \, dA}{\frac{1}{2}\rho U^2 A} = \frac{\int C_p \cos\theta \, dA}{A} \tag{9.23}$$

Here $C_p = (p - p_0)/(\rho U^2/2)$ is the *pressure coefficient*, where p_0 is a reference pressure. The level of the reference pressure, p_0, does not influence the drag directly because the net pressure force on a body is zero if the pressure is constant (i.e., p_0) on the entire surface.

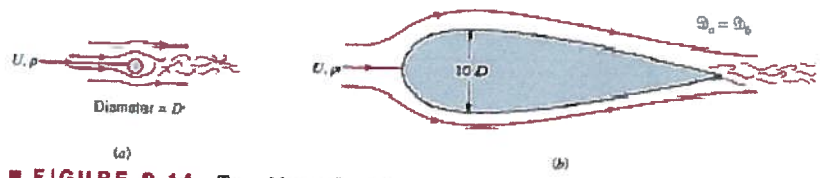

■ **FIGURE 9.14** Two objects of considerably different size that have the same drag force: (*a*) circular cylinder $C_D = 1.2$, (*b*) streamlined strut $C_D = 0.12$.

Reynolds Number Dependence. Another parameter on which the drag coefficient can be very dependent is the Reynolds number. Low Reynolds number flows (Re < 1) are governed by a balance between viscous and pressure forces. Inertia effects are negligibly small. In such instances the drag is expected to be a function of the upstream velocity, U, the body size, ℓ, and the viscosity, μ. That is,

$$\mathcal{D} = f(U, \ell, \mu)$$

From dimensional considerations (see Section 7.7.1)

$$\mathcal{D} = C\mu\ell U \tag{9.24}$$

where the value of the constant C depends on the shape of the body. If we put Eq. 9.24 into dimensionless form using the standard definition of the drag coefficient, $C_D = \mathcal{D}/\frac{1}{2}\rho U^2 A$, we obtain

$$C_D = \frac{\text{constant}}{\text{Re}}$$

where $\text{Re} = \rho U\ell/\mu$. For a sphere it can be shown that $C_D = 24/\text{Re}$, where $\ell = D$, the sphere diameter. For most objects, the low Reynolds number flow results are valid up to a Reynolds number of about 1.

EXAMPLE 9.5

A small grain of sand diameter $D = 0.10$ mm and specific gravity $SG = 2.3$ settles to the bottom of a lake after having been stirred up by a passing boat. Determine how fast it falls through the still water.

SOLUTION

A free-body diagram of the particle (relative to the moving particle) is shown in Fig. E9.5. The particle moves downward with a constant velocity U that is governed by a balance between the weight of the particle, $\mathcal{W}$, the buoyancy force of the surrounding water, F_B, and the drag of the water on the particle, $\mathcal{D}$.

From the free-body diagram we obtain

$$\mathcal{W} = \mathcal{D} + F_B$$

■ FIGURE E9.5

where

$$\mathcal{W} = \gamma_{sand}\mathcal{V} = SG\,\gamma_{H_2O}\frac{\pi}{6}D^3 \tag{1}$$

and

$$F_B = \gamma_{H_2O}\mathcal{V} = \gamma_{H_2O}\frac{\pi}{6}D^3 \tag{2}$$

We assume (because of the smallness of the object) that the flow will be creeping flow ($Re < 1$) with $C_D = 24/Re$ so that

$$\mathcal{D} = \frac{1}{2}\rho_{H_2O}U^2\frac{\pi}{4}D^2C_D = \frac{1}{2}\rho_{H_2O}U^2\frac{\pi}{4}D^2\left(\frac{24}{\rho_{H_2O}UD/\mu_{H_2O}}\right)$$

or

$$\mathcal{D} = 3\pi\mu_{H_2O}UD \tag{3}$$

We must eventually check to determine if this assumption is valid or not. Equation 3 is called Stokes law in honor of G. G. Stokes, a British mathematician and a physicist. By combining Eqs. 1, 2, and 3, we obtain

$$SG\,\gamma_{H_2O}\frac{\pi}{6}D^3 = 3\pi\mu_{H_2O}UD + \gamma_{H_2O}\frac{\pi}{6}D^3$$

or, since $\gamma = \rho g$,

$$U = \frac{(SG\rho_{H_2O} - \rho_{H_2O})gD^2}{18\mu} \tag{4}$$

From Table 1.5 for water at 15.6 °C we obtain $\rho_{H_2O} = 999\ \text{kg/m}^3$ and $\mu_{H_2O} = 1.12 \times 10^{-3}$ N·s/m². Thus, from Eq. 4 we obtain

$$U = \frac{(2.3 - 1)(999\ \text{kg/m}^3)(9.81\ \text{m/s}^2)(0.10 \times 10^{-3}\ \text{m})^2}{18(1.12 \times 10^{-3}\ \text{N·s/m}^2)}$$

or

$$U = 6.32 \times 10^{-3}\ \text{m/s} \qquad \text{(Ans)}$$

Proc. Symp. Soil Behavior and Soft Ground Construction, in honor of Charles C. Ladd - October 2001, MIT

Soil Behavior at the Microscale: Particle Forces

J. Carlos Santamarina[1]

Abstract

Soils are particulate materials. Therefore, the behavior of soils is determined by the forces particles experience. These include forces due to boundary loads (transmitted through the skeleton), particle-level forces (gravitational, buoyant, and hydrodynamic), and contact level forces (capillary, electrical and cementation-reactive). The relative balance between these forces permits identifying various domains of soil behavior. Furthermore, the evolution of particle forces helps explain phenomena related to unsaturation, differences between drained and undrained strength under various loading modes (including the effect of plasticity), sampling disturbance, and fines migration during seepage. Generally accepted concepts gain new clarity when re-interpreted at the level of particle forces.

Introduction

The limitations with continuum theories for the analysis of soil behavior were recognized early in the twentieth century. Terzaghi wrote "... Coulomb... purposely ignored the fact that sand consists of individual grains, and ... dealt with the sand as if it were a homogeneous mass with certain mechanical properties. Coulomb's idea proved very useful as a working hypothesis for the solution of one special problem of the earth-pressure theory, but it developed into an obstacle against further progress as soon as its hypothetical character came to be forgotten by Coulomb's successors. The way out of the difficulty lies in dropping the old fundamental principles and starting again from the elementary fact that sand consists of individual grains" (Terzaghi 1920 - includes references to previous researchers).

The fundamental understanding of soil behavior begins by recognizing the particulate nature of soils and its immediate implications: the interplay between particle characteristics (e.g., size, shape, mineralogy), inter-particle arrangement and interconnected porosity, inherently non-linear non-elastic contact phenomena, and

[1] Professor, School of Civil and Environmental Engineering, Georgia Institute of Technology, Atlanta, GA 30332. E-mail: carlos@ce.gatech.edu.

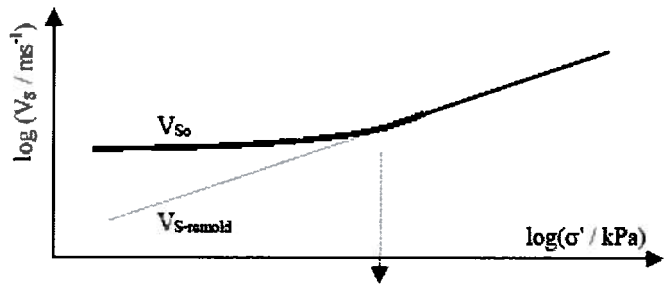

	Cement-controlled behavior $V_{So} > V_{S\text{-remold}}$	Stress-controlled behavior $V_{So} \approx V_{S\text{-remold}}$
No debonding $\Delta\sigma' < \Delta\sigma'_{debond}$	No sampling effect (sandstone at shallow depth)	No sampling effect (weakly cemented soil at depth)
Debonding $\Delta\sigma' > \Delta\sigma'_{debond}$.	stress reduction during sampling affects the measured properties	No sampling effect (soil debonds, but behavior is determined by σ')

Figure 9. Skeletal forces vs. cementation strength – Sampling and debonding.

and in the field (Tatsuoka and Shibuya 1992; Leroueil, 2001; data by Stokoe published in Stokoe and Santamarina 2000).

In line with the main emphasis of this manuscript, the preceding analysis was done in terms of contact forces and stress reduction. Alternatively, the analysis can be generalized in terms of strains (or particle-level deformation) and compared against the linear and degradation threshold strain of the soil. Stress reduction is the prevailing mechanism in block sampling; with other samplers, insertion and removal of the specimens cause additional stresses, pore pressure changes and volume changes in the soil that must also be taken into consideration.

Drag Force, Weight and Electrical Forces - Fines Migration

The potential for fines migration during seepage depends on the balance between the drag force, the weight of the particle and other resisting contact forces. Figure 10 shows the drag force for different pore flow velocities in comparison with the sum of the weight and the van der Waals attraction (computed for a possible Rep-Att minimum at 30 Å and at 100 Å inter-particle distances). Notice that:

- The migration of particles greater than about 100 μm is unlikely (the required pore flow velocity would render a turbulent regime).
- The migration of particles less than ~10 μm is determined by the electrical forces. In this case, changing the pore fluid chemistry can alter the force balance. For

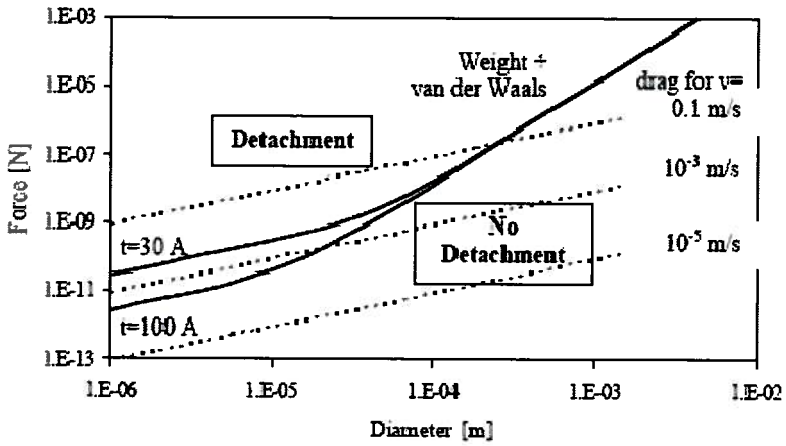

Figure 10. Drag vs. weight and net electrical attraction force.

example, a low concentration front may promote massive particle detachment allowing for particle migration.

- While individual small particles may not be detached, flocks of particles may.

For the conditions considered in the figure, a minimum pore flow velocity $v \approx 10^{-3}$ m/s is needed to cause detachment of any particle. Such pore flow velocity can be attained in sands or in coarse silts at high gradients. Therefore movable particles or "fines migration" is only relevant in the coarser formations and at high gradients, such as near a well.

Particles that are dragged may be flushed out of the soil or may form bridges at pore throats clogging the soil. Flushing and clogging depend on the relative size of the pore throats between skeleton-forming particles d_{large}, the size of the smaller migrating particles d_{small}, their ability to form bridges, and the volumetric concentration of fines in the permeant (Valdes 2002). In general, the required condition for flushing to occur is $d_{large}/d_{small} > 15$-to-30. These microscale considerations provide insight into filter criteria. Whether flushing or clogging develops, the movement of the movable particles renders fluid flow non-linear, causing pressure jumps and changes in effective stress.

Skeletal Force Distribution: Effective Stress Strength (Friction Angle)

Micromechanical analyses and simulations show the relevance of particle coordination, rotational frustration and the buckling of chains on the ability of a soil to mobilize internal shear strength (Figures 1, 2 and 3). Such analyses predict that: (1) the friction angle is highest in plane strain, then in axial extension, and least in axial compression, (2) the difference in peak friction between plane strain and AC increases with inter-particle friction and density due to the enhanced rotational frustration, and (3) the difference among critical state friction angles determined at different b-values is smaller than among peak friction values. All these